NUMERICAL INVESTIGATION OF THE POST-SHOCK REGION OF TRANSONIC BUFFET

Thomas Lürkens, Matthias Meinke, Dominik Krug
Institute of Aerodynamics and Chair of Fluid Mechanics
RWTH Aachen University
Wüllnerstr 5a, 52062 Aachen, Germany
{t.luerkens, m.meinke, d.krug}@aia.rwth-aachen.de

Wolfgang Schröder
Institute of Aerodynamics and Chair of Fluid Mechanics &
JARA Center for Simulation and Data Science RWTH Aachen University
Wüllnerstr 5a, 52062 Aachen, Germany
office@aia.rwth-aachen.de

ABSTRACT

Wall-resolved large-eddy simulations of the OAT15A airfoil are performed at buffet conditions, i.e., the freestream Reynolds number is $Re_\infty = 750\,000$, the freestream Mach number is $Ma_\infty = 0.73$ and the angle of attack is $\alpha = 3.5°$. Two Cartesian grid configurations are considered. The first configuration features only local refinement in the immediate region around the shock, whereas the second configuration has continuous mesh refinement from the shock to the trailing edge. This allows the influence of the downstream refinement extent on the resolved flow dynamics and outer-flow coupling to be examined.

Significant differences between both simulations are observed in the low-frequency oscillation of the shock wave and the resulting fluctuation of the lift coefficient. Spectral analysis of the trailing-edge and outer-flow pressure signals suggests that pressure waves propagating from the trailing edge toward the shock alone are not sufficient to sustain the low-frequency shock motion. Instead, analysis of the turbulent boundary layer downstream of the shock indicates a strong sensitivity of the trailing-edge separation behavior, which is closely linked to turbulent momentum transport within the boundary layer.

INTRODUCTION

The transonic buffet phenomenon refers to low-frequency self-sustaining oscillations of shock waves on airfoils and wings. These oscillations occur in transonic flow under specific combinations of Mach number and angle of attack. The oscillating shock wave exerts considerable fluctuating loads on the wing, which adversely affects the integrity of the structure. Therefore, a thorough understanding of the underlying physical mechanisms is crucial for the design of highly efficient lightweight aircraft. However, despite significant efforts by the research community, the driving forces behind the self-sustaining nature of the shock oscillation are still the subject of ongoing research.

One explanation was proposed by Lee (2001), who considered a closed feedback loop between the shock and the trailing edge. The proposed mechanism is based on the generation of vortices from the interaction of the boundary layer with the shock wave. When passing over the trailing edge the transition from a wall-bounded to a free-shear layer leads to the generation of pressure waves, so-called Kutta waves, which propagate upstream. The interaction of these pressure waves with the shock pushes the shock upstream leading to an increased relative Mach number between the shock and the incoming flow. As a result, the pressure jump across the shock increases and the boundary layer behind the shock thickens progressively until eventually the flow separates. At this point, the vortices detach from the airfoil and no longer pass the trailing edge. The generation of Kutta waves collapses. This allows the shock to move back downstream until the boundary layer reattaches to the surface, reestablishing the generation of Kutta waves, and thus closing the feedback loop (Lee, 2001). Lee's approach was reformulated by Hartmann *et al.* (2013). Instead of the shock foot, the tip of the shock was considered to be the critical point of interaction with the upstream propagating pressure waves triggering the upstream movement of the shock. Thereby, the prediction of the cycle duration resulting from the downstream convection velocity of the vortices and the upstream propagation velocity of the pressure waves with respect to the according distances could be improved (Hartmann, 2013).

Fundamental to the buffet models is the intermittent propagation of pressure waves from the trailing edge to the shock and the state of the boundary layer at the trailing edge. This motivates the present study, which will provide a detailed analysis of the propagation behavior in the region downstream of the shock, its relation to the vortical structures passing over the trailing edge, and the instantaneous state of the boundary layer.

NUMERICAL METHOD

The simulations presented are performed with the Cartesian solver of the open-source multiphysics simulation framework m-AIA (Institute of Aerodynamics, RWTH Aachen University (2024)), which solves the compressible, unsteady Navier-Stokes equations on a hierarchical Cartesian mesh by

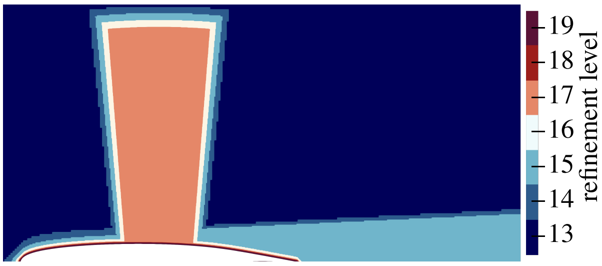

(a) Localized shock refinement (LR)

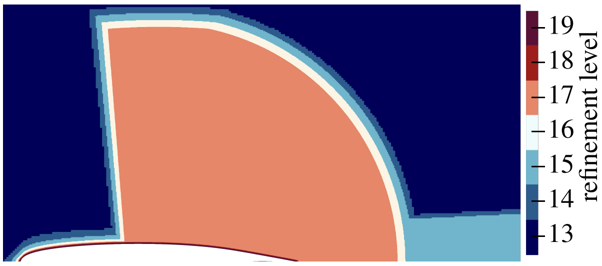

(b) Extended shock refinement (ER)

Figure 1: Contours of the refined mesh regions on the suction side.

the finite-volume method. Primitive variables on cell surfaces are extrapolated using a MUSCL scheme. The convective fluxes are approximated by the advective upstream splitting method (AUSM) allowing the accurate capturing of shock waves. At isotropic grid regions, the scheme is upwind-biased with an upwind coefficient of $\chi = 0.01$. For surfaces with a level jump between their respective neighbors, the upwind coefficient is set to $\chi = 0.5$. Thereby, numerical oscillations across refinement boundaries are mitigated at the cost of reduced preservation of sharp gradients. The viscous fluxes are discretized by a central difference scheme. A 5-stage Runge-Kutta method is employed for the temporal integration such that the overall discretization is of second-order accuracy in space and time. The effects of subgrid-scale turbulence are accounted for following the approach of monotone integrated LES (MILES, Boris *et al.* (1992)), which means that, following Meinke *et al.* (2002), no explicit subgrid-scale model is necessary. Embedded bodies are realized using the Cartesian cut-cell method from Schneiders *et al.* (2016).

SIMULATION SETUP

The setup is based on the well-established supercritical OAT15A airfoil with a blunt trailing edge of thickness $0.005c$, where c is the chord length. The simulations are conducted at a chord-based Reynolds number $Re_c = 750000$, freestream Mach number $Ma_\infty = 0.73$, and angle of attack $\alpha = 3.5°$. The tripping method by Schlatter & Örlü (2012) is applied at $x/c = 0.07$ on the suction side of the airfoil to force a transition of the boundary layer to turbulence. The pressure side of the airfoil is left without any boundary layer tripping applied.

The mesh was generated using the Cartesian mesh generator from the m-AIA simulation framework. The global mesh dimensions are given by $L_x \times L_y \times L_z = 61.5c \times 61.5c \times 0.03c$. To take into account the strong influence of the shock on the far-field, the profile was not centered within these boundaries, but placed with an offset of about $10.5c$ downstream and towards the pressure side of the airfoil.

Mesh refinement of the boundary layer and the wake region was applied a priori. The shock region was refined at runtime once an interim stable solution was established. Two strategies of shock refinement were applied. In the first case, the mesh refinement is limited to the immediate area around the shock wave. This case of only localized mesh refinement will be denoted LR. In the other case, the mesh is refined from a few percent upstream of the shock down to the trailing edge. This case of extended mesh refinement will be referred to as ER. It goes without saying that the different refinements do have an impact on the flow structures especially downstream of the shock. Note that the near-wall resolution of the boundary layer is consistent across both configurations. Illustrations of the refinement areas around the shock and trailing edge are shown in figures 1a and 1b. The uniform mesh size in the far-field is $\Delta_c/c = 0.0075$. In the respective shock refinement regions the mesh size is given by $\Delta_c/c = 4.692 \cdot 10^{-4}$. Wall surfaces are refined down to a cell size of $\Delta_c/c = 1.173 \cdot 10^{-4}$. The size of the smallest isotropic Cartesian cells in the near-wall region is given in Figure 2 showing a grid resolution of $\Delta_c^+ \approx 3.5$ upstream of the shock. The total mesh size sums up to $568 \cdot 10^6$ cells for the LR case and to $697 \cdot 10^6$ cells for the ER case.

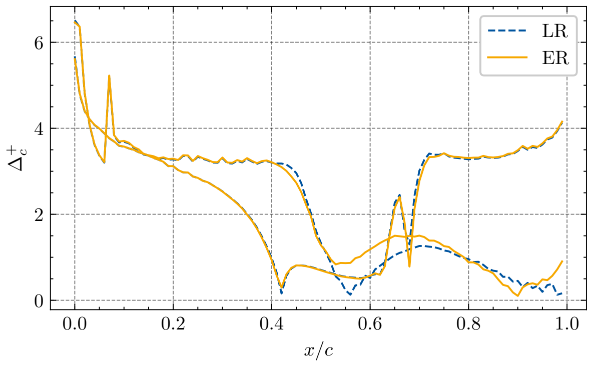

Figure 2: Cell size in inner units on the finest level in the near-wall region.

RESULTS

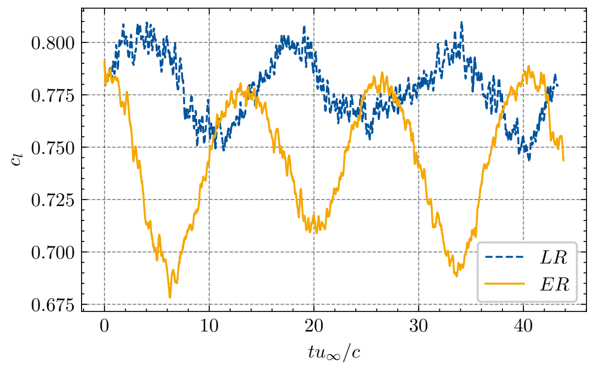

Figure 3: Time series of the lift coefficient of the LR and ER configurations.

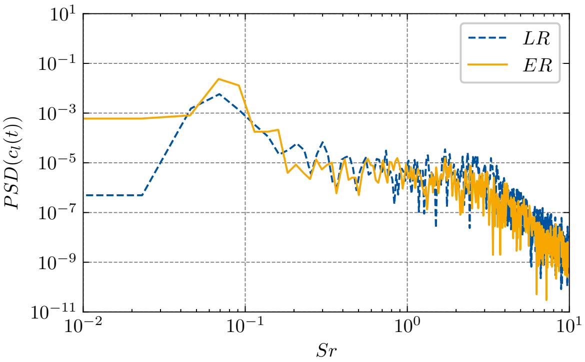

Figure 4: Power spectral density of the lift coefficient.

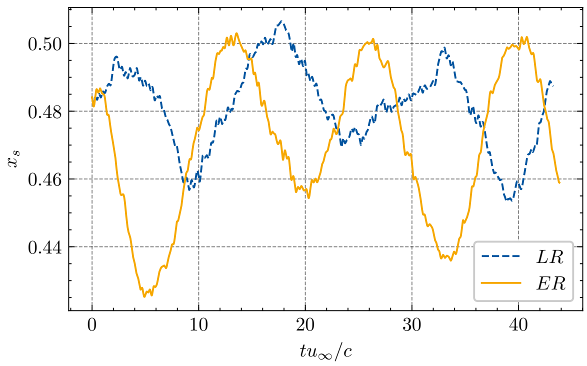

Figure 5: Time series of the shock position of the LR and ER configurations.

The impact of the different refinement strategies on the resulting flow structures will be examined for both grid configurations. The temporal evolution of the lift coefficient covering approximately three full buffet cycles is given in Figure 3. It is evident that the ER configuration is subject to significantly increased amplitudes in the lift oscillation and undergoes a notable drop in the mean lift compared to the LR configuration. Furthermore, the lift oscillation of the LR configuration exhibits a visibly higher degree of irregularity. The frequency spectrum of the lift coefficient is given in Figure 4 confirming the increased amplitude of the buffet in the ER configuration which is found for a non-dimensional frequency of $Sr \approx 0.07$, where the Strouhal number is given by $Sr = fc/u_\infty$. The unevenness in the lift oscillation of the LR configuration is reflected in a much broader low-frequency peak.

In Figure 5, the corresponding time series of the shock position determined as the chordwise coordinate with the steepest slope of the surface pressure coefficient is shown. The increased amplitude in the lift coefficient observed in the ER configuration is reflected in a larger amplitude of the shock position. However, while the most downstream shock position is mostly maintained across both configurations, the corresponding maximum lift coefficient is decreased in the ER configuration indicating a more fundamental change to the flow topology.

To examine the influence of the grid configurations on the fluctuating generation of Kutta waves at the trailing edge and the propagation to the outer flow region, the time-resolved premultiplied power spectrum of the mean-subtracted pressure signal at the trailing edge ($x/c = 0.99; y_n/c = 0.0$) and at a point in the outer flow region downstream of the shock ($x/c = 0.7; y_n/c = 0.3$) is computed using the continuous wavelet transform (CWT, Daubechies (1992)). The quantity x denotes the chord-wise coordinate on the surface of the airfoil suction side and y_n the wall-normal distance to that point. In Figures 6a and 6b the trailing-edge spectra are shown. In the low-frequency band around $Sr = 0.07$, the buffet frequency is dominant and significantly more pronounced in the ER configuration. In contrast, the frequency band around Strouhal numbers from 2 to 4 is significantly more pronounced in the LR configuration. Schauerte & Schreyer (2023) associated this frequency range with coherent structures originating from the shock-wave/boundary-layer interaction and convecting over the trailing edge into the free shear layer. The findings from the trailing edge spectra are reflected in the spectra from the outer flow region shown in Figures 6c and 6d. That is, the ER configuration exhibits stronger peaks in the buffet frequency, whereas the spectrum of the LR configuration is more pronounced in the frequency range $Sr = 2$ to 4.

To quantify the transmissability of the pressure fluctuations from trailing edge to the outer region the transfer function $H_{TE,o} = S_{TE,o}/S_{TE,TE}$ is computed, where $S_{TE,o}$ is the cross-spectrum of the trailing-edge and the outer-region pressure signal and $S_{TE,TE}$ is the auto-spectrum of the trailing-edge signal. Frequencies showing low coherence $C_{TE,o} < 0.3$ between the signals were filtered out. In Figure 7, the gain defined as the magnitude of the transfer function is shown. For $Sr > 7$, a clear deviation between the configurations is observed, where the ER configuration exhibits higher transmission of pressure fluctuations than the LR case. In contrast, for the frequency range associated with the large scale-structures passing over the trailing edge, i.e. $2 < Sr < 4$, no significant differences in the transmission behavior are found.

From Figure 3 and Figure 5 it is evident that although the most downstream shock position is maintained across both configurations, the corresponding lift coefficient decreases significantly in the ER configuration. To investigate this discrepancy, the boundary layer downstream of the shock is examined. The mean skin-friction coefficient downstream of the shock is given in Figure 8, where the shaded area indicates the range between the first and the third quartiles of the time series. Immediately downstream of the shock, the ER configuration shows an overall higher fluctuation range in the skin friction which can be associated with the stronger oscillation of the shock. At the trailing edge, however, the LR configuration exhibits stronger fluctuations. Furthermore, in the temporal mean, the ER configuration shows clear trailing-edge separation, whereas the LR configuration remains close to zero. This difference in the trailing-edge flow accounts for the observed differences in the lift coefficient between the two configurations at matching shock positions.

Figure 9 shows the joint distribution of the wall-tangential and wall-normal components of the velocity fluctuation in the boundary layer at $x/c = 0.8; y_n/c = 0.025$. Compared to the ER configuration, the distribution of the LR configuration is significantly more tilted towards $u'v' < 0$ indicating enhanced transport of high-momentum fluid from the outer layer towards the wall and low-momentum fluid from the near-wall region towards the outer layer. The increased redistribution of momentum within the boundary layer in the LR configuration explains the different separation behavior at the trailing edge observed in Figure 8.

To gain further insight into the structure of the turbulent boundary layer, a two-dimensional snapshot sequence of the (u, v) velocity field was decomposed using the two-dimensional noise-assisted multivariate empirical mode decomposition (2D NA-MEMD), as introduced by Mäteling &

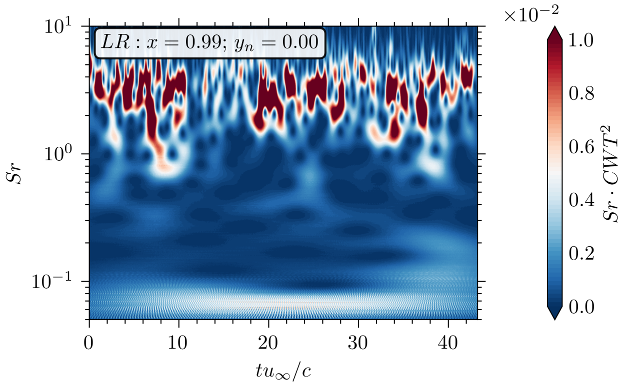

(a) LR, trailing edge: $x/c = 0.99$; $y_n/c = 0.0$

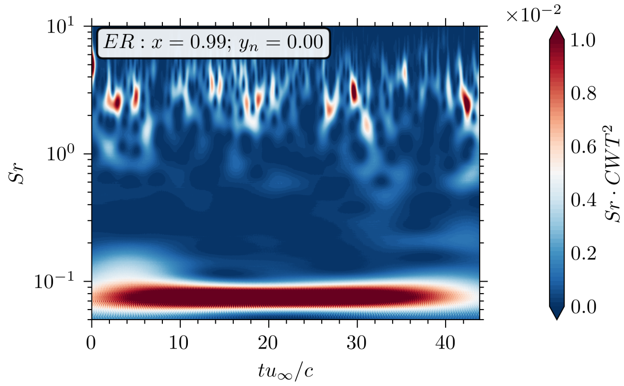

(b) ER, trailing edge: $x/c = 0.99$; $y_n/c = 0.0$

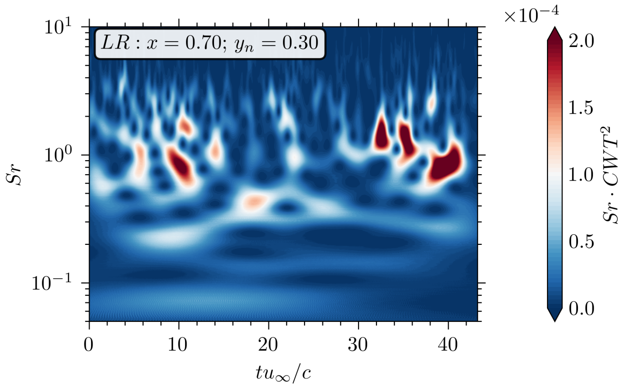

(c) LR, outer flow: $x/c = 0.70$; $y_n/c = 0.30$

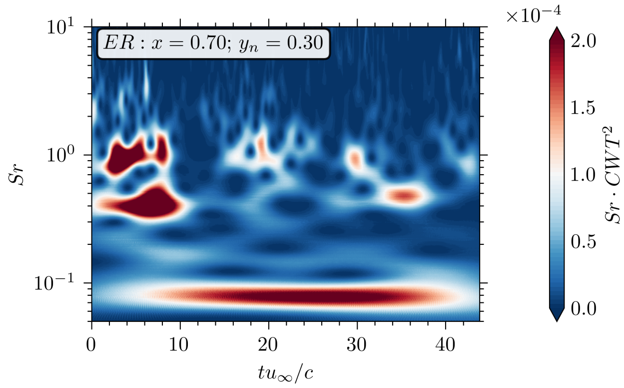

(d) ER, outer flow: $x/c = 0.70$; $y_n/c = 0.30$

Figure 6: Time-resolved premultiplied power spectrum of the mean subtracted pressure signal computed using a continuous wavelet transform (CWT).

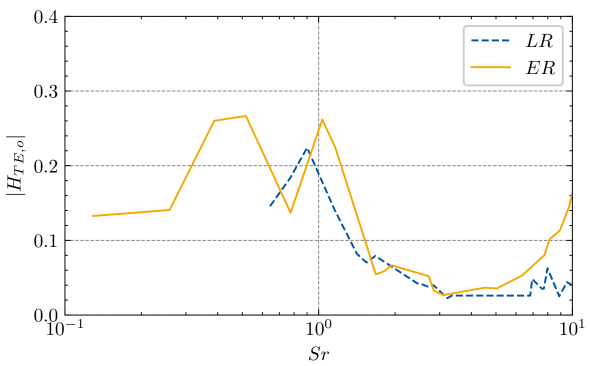

Figure 7: Transfer function of the pressure signal at the trailing edge to the pressure signal in the outer flow region.

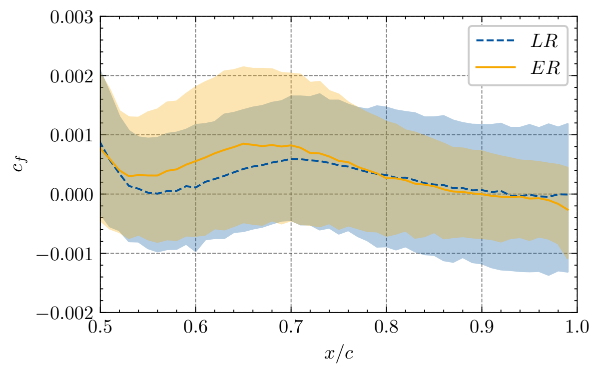

Figure 8: Mean skin-friction coefficient on the suction side downstream of the shock. Shaded area marks the bounds of the first and third quartile of the temporal variation.

Schröder for the analysis of inner–outer layer interactions in turbulent wall-bounded flows. The 2D NA-MEMD decomposes a two-dimensional multivariate data field into a set of intrinsic mode functions (IMFs) and is particularly suitable for the analysis of non-linear fields owing to its data adaptive nature. The determination of the IMFs is based on the construction of upper and lower envelope surfaces of the multivariate data field. The IMFs are then computed iteratively by subtracting the mean of the upper and lower envelopes from the residual data field. The resulting decomposition provides insight in the structure of the boundary layer at the characteristic length scale of the respective IMF. For further information on the algorithm the reader is referred to the work of Mäteling & Schröder (2022). In total five IMFs were extracted from each individual snapshot. The temporally averaged energy of the individual IMFs is computed by

$$E_m = \frac{1}{N} \sum_{n=1}^{N} \sum_{i,j} \left((u_{i,j}^{(n,m)})^2 + (v_{i,j}^{(n,m)})^2 \right), \qquad (1)$$

where m is the index of the IMF, N is the number of snapshots, and (i, j) is the index of the structured grid. The energy

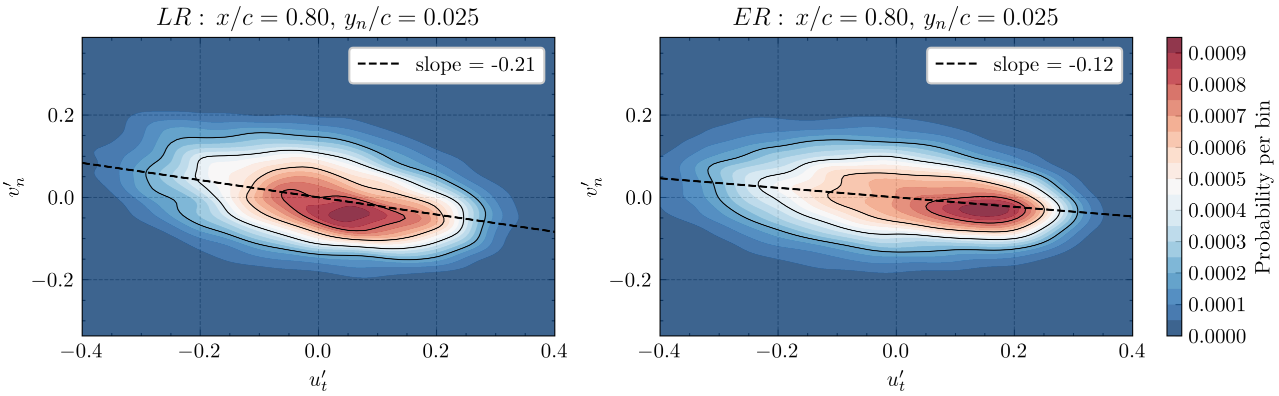

Figure 9: Probability distribution of the velocity fluctuations in the boundary layer at $x/c = 0.8$ and $y_n/c = 0.025$. The dashed line represents a linear regression fit.

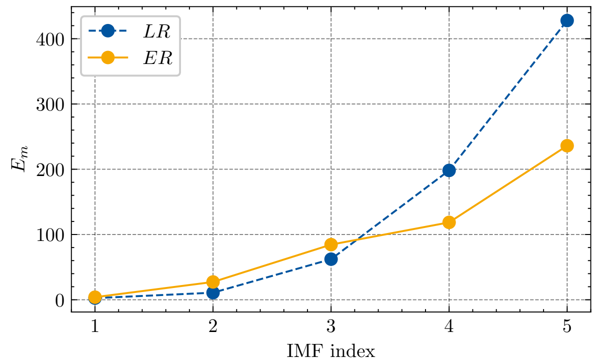

Figure 10: Energy distribution across IMFs.

distribution across the IMFs for both configurations is given in Figure 10 showing a significant increase in energy in the large-scale IMFs 4 and 5 and lower energy in the small-scale modes 2 and 3 for the LR configuration.

In Figures 11a and 11b instantaneous contours of the IMFs of the streamwise velocity component are shown at the respective most upstream shock position. Based on the observed differences in the energy distribution across the modes, the first and second IMFs, representing the smallest turbulent scales, and the fourth and fifth IMFs, representing the larger scales, are grouped for further analysis. It is evident that turbulent structures downstream of the shock–wave/boundary-layer interaction are significantly affected when passing the mesh refinement interface in the outer region downstream of the shock, particularly in IMFs 1 and 2 of the LR configuration. These structures appear to undergo a redistribution to more coherent larger scales which is reflected by the increased energy in IMFs 4 and 5. The presence of more pronounced large-scale structures passing over the trailing edge can be associated with the stronger pressure fluctuations at the trailing edge observed for the LR configuration in Figure 6 and the larger fluctuative range of the skin-friction coefficient in Figure 8. Furthermore, the residual data field shown in the bottom panels of Figure 11, representing the large-scale flow structure, exhibits more extensive low-momentum regions at the trailing edge.

Since each IMF represents a fluctuating component at a specific spatial scale, its contribution to turbulent momentum transport can be defined as

$$(u'v')_m = IMF_m(u) \cdot IMF_m(v). \tag{2}$$

Figure 12 shows the difference $\Delta(\overline{u'v'})_m = (\overline{u'v'})_m^{LR} - (\overline{u'v'})_m^{ER}$ in large-scale turbulent momentum transport (IMFs 4 + 5) between the LR and ER configurations, averaged over the snapshot sequence. Therefore, the increased turbulent momentum transport towards the wall observed in Figure 9 can be attributed to the artificially increased energy in the large-scale structures caused by the mesh refinement jump behind shock.

Furthermore, the power spectral density of large-scale velocity fluctuations, computed from the temporal development of IMFs 4 and 5 at $(x/c = 0.95,, y_n/c = 0.025)$, is shown in Figure 13. The LR configuration exhibits a pronounced increase in energy in the Strouhal number range $Sr = 2$ to 4, consistent with the elevated trailing-edge and outer-flow pressure spectra previously observed in Figure 6. This increase in trailing-edge pressure fluctuations in this frequency band can be linked to the enhanced large-scale flow structures in the LR configuration.

CONCLUSION

Wall-resolved large-eddy simulations of the OAT15A airfoil were performed at buffet conditions using two different grid configurations. One configuration features local mesh refinement only in the immediate vicinity of the shock, whereas the other configuration extends the refined region from the shock to the trailing edge. Significant differences between both simulations are observed in the low-frequency oscillation of the shock wave, where only the configuration with extended refinement exhibits well-developed shock buffet.

Despite its weaker manifestation of shock buffet, analysis of the frequency spectra of the trailing-edge and outer-flow pressure signals reveals stronger fluctuations for the LR configuration. Further examination of the wall-bounded flow shows that the ER configuration, which exhibits well-developed shock buffet, is characterized by significantly more consistent trailing-edge separation. This difference in trailing-edge separation can be linked to an artificially modified turbulent momentum transport in the LR configuration, associated with large-scale turbulent structures identified using 2D NA-MEMD.

The opposing behavior of the shock oscillation amplitude and the generation of Kutta waves indicates that the upstream propagation of pressure waves from the trailing edge is not sufficient to govern the correct development of shock buffet. Instead, the importance of the boundary-layer state at the trailing edge is highlighted, which is highly sensitive to the adequate resolution of small-scale turbulence originating from the

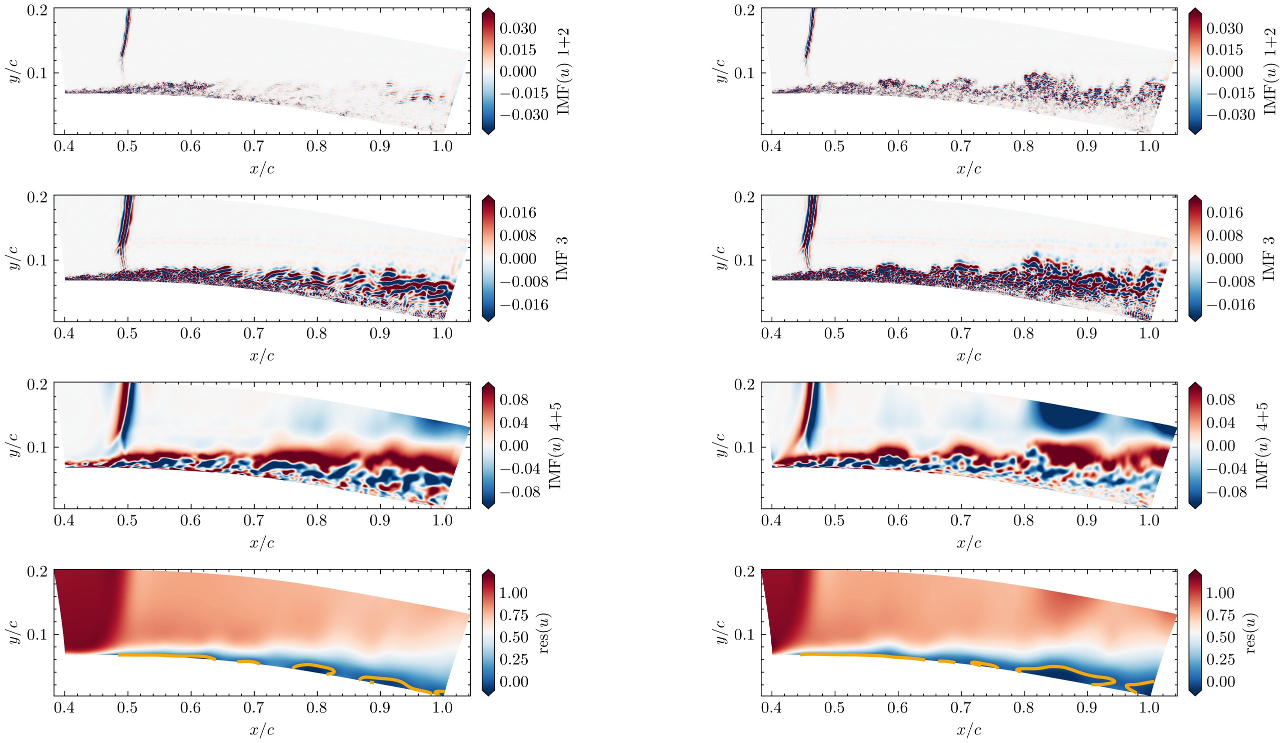

(a) Local refinement (LR) (b) Extended refinement (ER)

Figure 11: Intrinsic mode functions (IMFs) of the streamwise velocity component computed using 2D NA-MEMD. Orange lines in the residual mark zero contours.

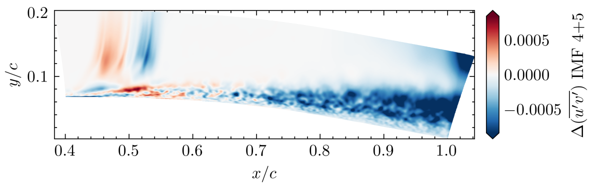

Figure 12: Difference in large-scale turbulent momentum transport towards the wall between the LR and ER configuration.

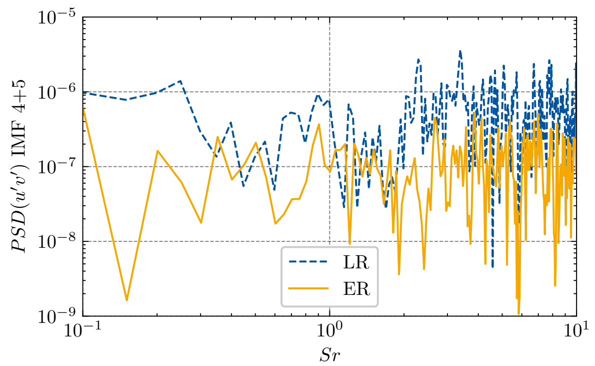

Figure 13: Power spectral density of IMF 4 + 5 in the boundary layer near the trailing edge $x/c = 0.95$, $y_n/c = 0.025$

shock-wave/boundary-layer interaction and the resulting momentum transport.

REFERENCES

Boris, J. P., Grinstein, F. F., Oran, E. S. & Kolbe, R. L. 1992 New insights into large eddy simulation. *Fluid Dynamics Research* **10** (4-6), 199–228.

Daubechies, I. 1992 *Ten Lectures on Wavelets*. Society for Industrial and Applied Mathematics.

Hartmann, A., Feldhusen, A. & Schröder, W. 2013 On the interaction of shock waves and sound waves in transonic buffet flow. *Physics of Fluids* **25** (2), 026101.

Institute of Aerodynamics, RWTH Aachen University 2024 m-AIA. Zenodo, doi:10.5281/zenodo.13350586.

Lee, B.H.K. 2001 Self-sustained shock oscillations on airfoils at transonic speeds. *Progress in Aerospace Sciences* **37** (2), 147–196.

Mäteling, E. & Schröder, W. 2022 Analysis of spatiotemporal inner-outer large-scale interactions in turbulent channel flow by multivariate empirical mode decomposition. *Phys. Rev. Fluids* **7**, 034603.

Meinke, M., Schröder, W., Krause, E. & Rister, Th. 2002 A comparison of second- and sixth-order methods for large-eddy simulations. *Computers & Fluids* **31** (4), 695–718.

Schauerte, Ch. & Schreyer, A.-M. 2023 Experimental investigation on the turbulent wake flow in fully established transonic buffet conditions. *CEAS Aeronautical Journal* **15**.

Schlatter, Ph. & Örlü, R. 2012 Turbulent boundary layers at moderate reynolds numbers: inflow length and tripping effects. *Journal of Fluid Mechanics* **710**, 5–34.

Schneiders, L., Günther, C., Meinke, M. & Schröder, W. 2016 An efficient conservative cut-cell method for rigid bodies interacting with viscous compressible flows. *Journal of Computational Physics* **311**, 62–86.